

Surface Termination-Dependent Nanotribological Properties of Single-Crystal MAPbBr₃ Surfaces

Joong Il Jake Choi,^{†,‡} Muhammad Ejaz Khan,^{§,⊥,‡,¶} Zafer Hawash,[⊥] Hyunhwa Lee,^{†,⊥,#} Luis

K. Ono,[⊥] Yabing Qi,^{*,⊥} Yong-Hoon Kim^{*,§,⊥} and Jeong Young Park^{*,†,⊥,#}

[†] Center for Nanomaterials and Chemical Reactions, Institute for Basic Science (IBS),
Daejeon 34141, Republic of Korea.

[§]School of Electrical Engineering, [⊥]Graduate School of Energy, Environment, Water, and
Sustainability, [#]Department of Chemistry, Advanced Institute of Science and Technology
(KAIST), Daejeon 34141, Republic of Korea.

[⊥]Energy Materials and Surface Sciences Unit (EMSSU), Okinawa Institute of Science and
Technology Graduate University (OIST), 1919-1 Tancha, Onna-son, Kunigami-gun,
Okinawa 904-0495, Japan.

[¶]Present address: School of Engineering Technology, National University of Technology, IJP
Road, Sector I-12, Islamabad 42000, Pakistan

*Address correspondence to Yabing.Qi@OIST.jp, y.h.kim@kaist.ac.kr,

jeongypark@kaist.ac.kr.

ABSTRACT

Atomistic characterization of surface termination and the corresponding mechanical properties of single-crystal methylammonium lead tribromide (MAPbBr₃) are performed using combined atomic force microscopy (AFM) measurements and density functional theory (DFT) calculations. A clean MAPbBr₃ surface is obtained by *in situ* cleavage in ultra-high vacuum at room temperature, and the subsequent AFM measurements of the as-cleaved MAPbBr₃ exhibit the coexistence of two different surface terrace types with step height differences corresponding to about half the thickness of a PbI₆ octahedron layer. Concurrent friction force microscopy measurements show that the two surfaces result in two distinct friction values. Based on DFT calculations, we attribute the higher-friction and lower-friction surfaces to MABr-terminated flat and PbBr₂-terminated vacant surface terminations, respectively. The calculated electronic band structures of the various MABr- and PbBr₂-terminated surfaces show that the mid-gap states are absent, revealing the defect-tolerant nature of the ideal single-crystal MAPbBr₃ surfaces.

INTRODUCTION

Methylammonium lead halides ($\text{CH}_3\text{NH}_3\text{PbX}_3$ or MAPbX_3 , $\text{X} = \text{Cl, Br, I}$) exhibit unique properties, including long carrier diffusion length,^{1,2} low charge recombination rates,^{3–5} shallow defect states,⁶ and high absorption coefficients for visible light. Due to such beneficial properties, hybrid perovskites find potential applications in photovoltaic cells (PSCs), light emitting diodes, and other optoelectronic device applications, with excellent device performance demonstrated at laboratory scale.^{7–13} Despite its significance in various applications, most of the studies into the properties of hybrid perovskites are conducted at device scale with a limited number of atomic-scale analyses. Consequently, the current understanding of the atomistic origins of the stability and degradation of perovskites mostly relies on theoretical studies with limited experimental evidence.^{14–18} Experimental investigation of the origins of the exceptional properties of hybrid perovskites at atomic scale would therefore provide valuable information for further development and precise design of highly efficient PSCs and other hybrid perovskite-based optoelectronic devices.

Investigation of the surface or the interface of highly-ordered model systems at atomic scale (e.g., studying single crystals in ultra-high vacuum (UHV)) is a key strategy for understanding the atomistic origin of the physical, chemical, and electronic properties of various materials.^{19–21} Recently, scanning probe microscopy has been used to explore the physical properties of the hybrid perovskites.^{22,23} However, although it would be a powerful technique that could provide information about local inhomogeneity and nanomechanical properties,²⁴ friction force microscopy study of hybrid perovskites has not been reported in the literature so far. In this paper, we report a combined atomic force microscopy (AFM)–density functional theory (DFT) investigation of *in situ* cleaved MAPbBr_3 single crystal in UHV. Herein, we identify inhomogeneities in MAPbBr_3 surface terminations that appear as nanotribological and topographical variations by carrying out AFM experiments. We

particularly identify two distinct friction features and assign the high- and low-friction surface compositions as the MABr-terminated flat and PbBr₂-terminated vacant surfaces, respectively. The mechanisms of the friction variations depending on the surface terminations and the corresponding surface electronic structures are clarified through DFT calculations. Clarifying the ideal initial surface conditions after the cleavage, we expect this work will pave the way for further atomic-scale studies of hybrid perovskites.

METHODS

Sample Fabrication and Preparation: A 1M solution of PbBr₂ (Sigma Aldrich, 98%) and MABr (Dyesol Ltd.) was prepared in dimethylformamide (DMF) at room temperature (24 °C) under ambient conditions. The precursors were dissolved, aided by ultra-sonication, for 30 min. After the precursors were completely dissolved, the solution was transferred to 5 ml vials of clear glass using a 0.22 μm pore size PTFE filter (2.5 ml of solution in each vial). Subsequently, the vials were placed in an oil bath at room temperature. The oil temperature was then increased slowly to reach 90 °C within 1 hour. After about 6 hours, seed crystals were observed to grow (often only 1 seed per vial was observed). For further crystal growth, the temperature was increased to 100 °C. The crystals were transferred to a new MAPbBr₃ solution to achieve even larger crystals.²⁵ A single-crystal MAPbBr₃ sample was cleaved in the load-lock of a UHV chamber (base pressure $\approx 10^{-8}$ Torr), similar to the method used by Ohmann *et al.*²² After cleavage, the sample was immediately transferred to the AFM chamber (base pressure $\approx 10^{-10}$ Torr).

Atomic Force Microscopy: Topography, friction, and conductance were obtained from contact-mode AFM (RHK UHV Beetle AFM/STM) measurements using a TiN-coated Si cantilever (CSG01, NT-MDT, typical force constant: $k = 0.03$ N/m).^{26–28} The radius of the tips was ≈ 10 nm, as specified by the manufacturer. For all the AFM images, the load at the

tip was virtually zero (i.e., the effective load was similar to the adhesion force between the tip and the sample, which is ≈ 3 nN). Since the image features and quality did not change over several repeated scans, we assume no damage occurred at the surface with this load.

Computational Details and Model Structures: DFT calculations were performed²⁹ as implemented in the Vienna Ab-initio Simulation Package^{30,31} within the generalized gradient approximation of Perdew–Burke–Erzenhof revised for solids (PBEsol).³² To crosscheck the reliability of the results, we performed additional calculations that include the effects of weak van der Waals interactions within the DFT-D3 method.³³ The core and valence electrons were handled by the projector augmented wave method.^{34,35} Plane-waves were expanded with a kinetic energy cutoff of 400 eV to obtain basis sets. A self-consistency cycle energy criterion of 10^{-4} eV was adopted. Atomic structures were optimized using the conjugate-gradient approach until the Hellmann–Feynman forces were less than 0.025 eV/Å.

We prepared various surface termination models for DFT calculations by considering a $2 \sim 4$ nm thick MAPbBr₃ slab. A vacuum space of more than 15 Å was inserted perpendicular to the direction of the slab surface to avoid interactions with neighboring images in the periodic boundary condition setup. Experimentally, the MAPbBr₃ perovskite has a cubic structure (*pm3m*) at room temperature with a lattice parameter of 5.90 Å.³⁶ The optimized lattice parameters used in our PBEsol and DFT-D3 calculations were comparable to the experimental values for bulk and slab structures (Supplementary Table S1). In the lateral directions, we considered a 2×2 MAPbBr₃(001) supercell with $4 \sim 6$ PbI₆ octahedron layers in the vertical direction, where the topmost layer could be a half-octahedra in some surface terminations. A $5 \times 5 \times 1$ *k*-point mesh was sampled in the Brillouin zone. To calculate the surface formation energies with more precise information determining the

surface stability, we used symmetric terminations at both sides of the slabs to avoid the possibility of an artificial net dipole moment in the supercell.

The stability of various surface terminations were determined by calculating their surface formation energies according to

$$\Delta\Omega = \frac{1}{2A_S} (E_S - N_S E_B / N_B), \quad (1)$$

where E_B and E_S are the DFT total energies of the relaxed MAPbBr₃ bulk and slab structural forms, respectively, N_B and N_S are the number of atoms in the bulk unit cell and slab supercell models, respectively, and A_S is the surface area of the slab.

We used bilayer tungsten (W) slab as a tip model placed about 0.34 nm above the surface to find the trend of the atomic-level lateral friction forces upon variations in the surface terminations (Fig. 3(b)). The W slab has a body centered cubic structure and we obtained a lattice constant of 2.86 Å optimized for the slab unit cell. In the force calculation setup, we used a 4 × 4 W supercell that has a small (< 3 %) lattice mismatch with 2 × 2 MAPbBr₃. The MAPbBr₃ lattice parameters were used for surface–tip geometry optimization. We fixed the top W layer and the bottom two layers of the MAPbBr₃ slab during geometry relaxation for the friction force calculations.

The lateral forces were computed based on the differences between the DFT total energies of the optimized crystal structures when the tip was placed at the initial and final positions with respect to the sliding displacement, according to

$$f_L = \frac{1}{n} \sum_{j=1}^n |(E_f - E_i) / (d_f - d_i)|, \quad (2)$$

where E_i and E_f are the DFT total energies of the relaxed MAPbBr₃ tip-slab structures with the tip at the d_i initial and d_f final positions, respectively. Equation (2) indicates that the energetically favorable sliding path on a particular surface termination leads to a small lateral

force f_L . Moreover, to compute the lateral forces, we scanned the surfaces by sliding the W-tip to a distance of about 25% of the lattice parameters along both paths I and II. More computational details can be found elsewhere.^{23,29}

RESULTS AND DISCUSSION

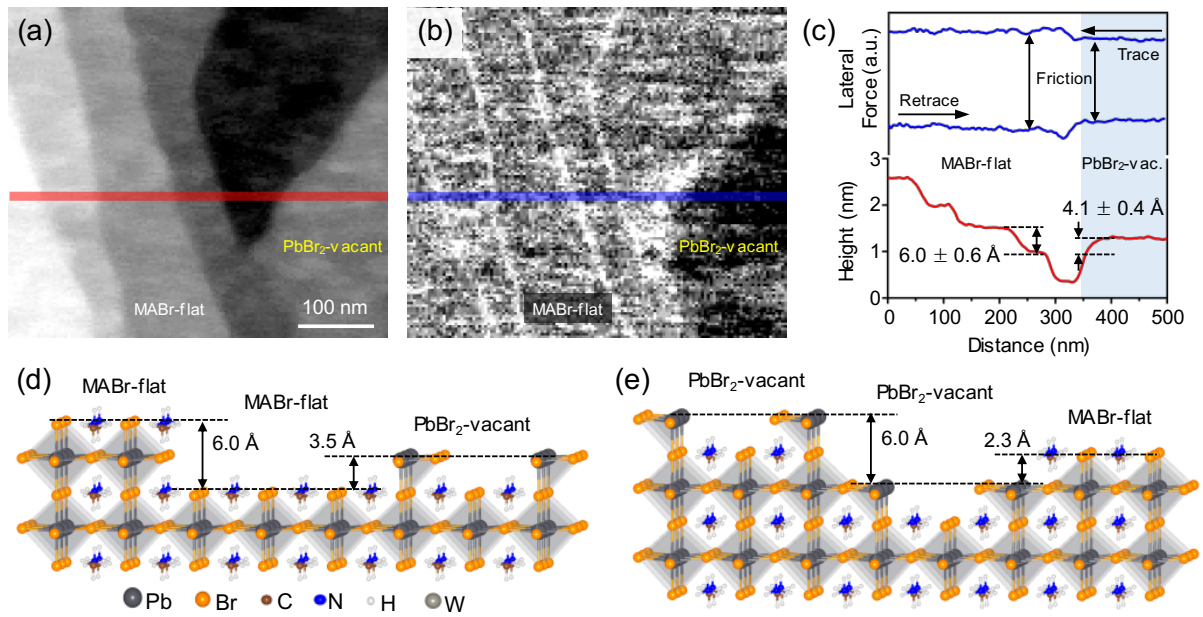


Figure 1. Contact-mode (a) topography and (b) lateral force AFM images of freshly cleaved single-crystal MAPbBr₃ showing large homogeneous terraces with distinctively different frictions. (c) Height (bottom) and lateral force (top) line profiles obtained from (a) and (b), as indicated by the red and blue lines, respectively. (d, e) Schematic illustrations of possible atomic step configurations explaining the lower layer height ($4.1 \pm 0.4 \text{ \AA}$) observed in the AFM topography.

Contact-mode AFM topography and lateral force images of the *in situ* cleaved MAPbBr₃ surface are shown in Figures 1(a) and 1(b), respectively. AFM measurements of the as-cleaved surfaces show the coexistence of two types of surface domains, one of which exhibits full atomic layer heights of the cubic perovskite structure of MAPbBr₃ (*i.e.* $\approx 6 \text{ \AA}$)³⁶, while the other shows lower heights ($\approx 4 \text{ \AA}$). In the majority of the area, we observe flat terraces larger than 300 nm with the single atomic step height of cubic MAPbBr₃, as shown in the

topography image (Figure 1(a)) and in the height profile (Figure 1(c)). Such domains show constant friction over several monolayer steps (see Figures 1(a) and (b), left area). On the other hand, the domain on the right side of Figure 1(b) exhibits a distinctively lower friction value. The corresponding lateral force line profiles are shown in Figure 1(c). We find the low-friction domain exhibits a notably lower step height compared with the cubic perovskite structure; the average height is $4.1 \pm 0.4 \text{ \AA}$. The distinct friction and step height clearly indicate different surface atomic structures for the two distinctive surface domains. Figures 1(d) and (e) show schematics of possible domain configurations for the two distinctive step heights observed in the AFM images. Previously, we identified two different stable surface terminations: (1) the MA-terminated flat surface based on a full octahedra layer (MABr-flat) and (2) the surface composed of distorted PbBr_2 tetrahedra and vacancies with a half octahedra layer height (PbBr_2 -vacant). Moreover, we demonstrated that even in the dark and low-humidity conditions, the most energetically stable MABr-flat surface can degrade into the thermodynamically preferred PbBr_2 -vacant surfaces.²³ Now, based on height profiles, both MABr-flat and PbBr_2 -vacant configurations schematically shown in Figures 1(d) and (e) can be utilized to explain the step height profiles in the AFM images. Based on covalent radii of the elements constituting the surfaces, we can estimate the height of PbBr_2 -vacant surface as $\approx 0.35 \text{ nm}$ with respect to the adjacent to MABr-flat surface. On the other hand, the height of the MABr-flat surface with respect to the bottom PbBr_2 -vacant surface would be only $\approx 0.23 \text{ nm}$. Namely, according to the experimental step height profile shown in Figure 1(c), we can assign the left high-friction and right low-friction domains to the MABr-flat and PbBr_2 -vacant surfaces, respectively (configurations in Figures 1(d) and (e)). DFT calculations of frictions of MABr-flat and PbBr_2 -vacant surfaces will confirm this assignment later.

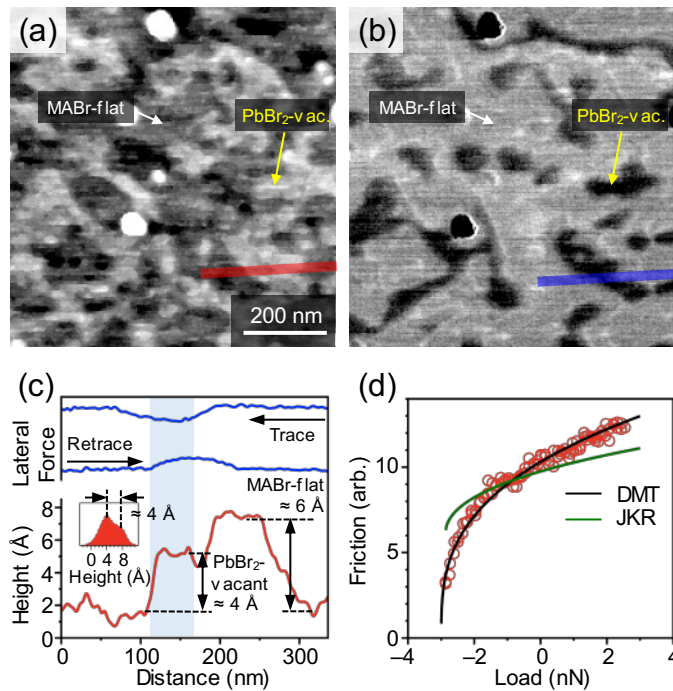


Figure 2. Contact-mode (a) topography and (b) lateral force AFM images of the inhomogeneous surface after cleavage of the MAPbBr₃ single crystal. In (b), dark areas correspond to lower friction regions, light areas to higher friction. (c) Lateral force (top) and topography (bottom) profiles from the red and blue lines in (a) and (b), respectively. The inset shows the height distribution from (a); the average height difference between the higher islands and the underlying terrace is ≈ 4 Å. (d) Load-dependent friction measured at the higher friction surface (i.e., lighter area in (b)). The data were fitted to the DMT and JKR elastic contact models; the DMT model provides a better fit.

In addition to the large terrace (either high-friction MABr-flat or low-friction PbBr₂-vacant surface) domains, we observed another area in which the low- and high-friction domains coexist and were randomly distributed as islands (see Figure 2(a)). We can hypothesize the creation of the two domains as following: the MABr-flat and PbBr₂-vacant domains are created randomly when cleaved and immediately form terraces around the step edges, but when the size of the terrace exceeds the diffusion length of the randomly dispersed domain fragments at room temperature, the domains agglomerate and form the disordered islands shown in Figure 2(a). Indeed, we mostly observed the disordered islands feature when the size of the terrace exceeded ≈ 1 μm (see Figure S1 for an example). It is worth noting that the formation of distinctive surface domains and the agglomeration to disordered islands after cleavage is

consistent with the surface morphology of as-cleaved oxide perovskite single crystals without strongly preferred cleavage planes.^{37–39} Figures 2(a) and (b) show images of the topography and lateral force (trace), respectively, that were obtained simultaneously. The line profile along the red and blue lines in the topography and lateral force images, respectively, are shown in Figure 2(c). In the height profile, we find the coexistence of 4 Å and 6 Å step heights; the 4 Å domain matches the area with lower friction, as indicated by the blue box in Figure 2(c). The slight offset between the lateral force scans in the trace and retrace directions originates from cantilever bending. Comparing the topography and friction images (i.e., Figures 2(a) and (b), respectively), we find that most, but not all, of the low-friction domains reside on the islands. This tendency can be explained by the higher density of the low-coordinated sites on the small islands preferentially creating the vacant structure (PbBr₂-vacant) at the step edges or on the islands, which can then reconstruct to form the low-friction domain. As a result, most of the low-friction domains are created on the islands, resulting in the average height of 4.0 Å for the islands, as shown in the height histogram (see the inset of Figure 2(c)).

We studied the mechanical characteristics of the surface domains using friction measurements as a function of load. Unfortunately, we could not differentiate the high-friction (6 Å) domain from the low-friction (4 Å) counterpart in the load-dependent friction measurements, mostly because the low-friction domain was easily damaged by the high load measurements. Figure 2(d) shows the load-dependent friction characteristics at the terrace with Johnson–Kendall–Roberts (JKR) and Derjaguin–Muller–Toporov (DMT) fittings with the adhesion force as a free parameter.^{40–42,24} The continuum mechanical theory can be used to describe the friction behavior. DMT and JKR models describe the two extreme cases of elastic contact, namely the rigid and poorly adhesive contact, and soft and highly adhesive contact, respectively. From the fitting, it is clear that the DMT fit complements the experimental data. The pull-off force, L_c , is -2.9 nN. Using $L_c = -2\pi\gamma R$, where R is the tip radius and γ is the

work of adhesion, from the DMT approximation, we find that $\gamma = 46 \text{ mJ/m}^2$. Often the inclination to either the DMT or JKR model is predicted by an empirical nondimensional parameter, the so-called Tabor parameter $\tau = \left(\frac{16R\gamma^2}{9K^2z_0^3}\right)$ where, z_0 is the equilibrium spacing of the two surfaces, and K is the combined elastic modulus of the two materials, given by $K = \left(\frac{4}{3}\right) \left[\frac{1-\nu_1^2}{E_1} + \frac{1-\nu_2^2}{E_2}\right]^{-1}$, where E_1 and E_2 are their Young's moduli and ν_1 and ν_2 are the Poisson ratios of the two respective materials in contact. One can expect the JKR model to accurately approximate the contact mechanism when $\tau > 5$, while DMT is expected to be accurate when $\tau < 0.1$. The Tabor parameter in the current case was found to be 0.18, using the tip radius, R , of 10 nm, $z_0 = 2 \text{ \AA}$, Young's moduli and Poisson ratios of MAPbBr₃ to be 19.6 GPa and 0.29,⁴³ and of TiN to be 600 GPa and 0.25, respectively, indicating that DMT model would better approximate the AFM tip–MAPbBr₃ contact.

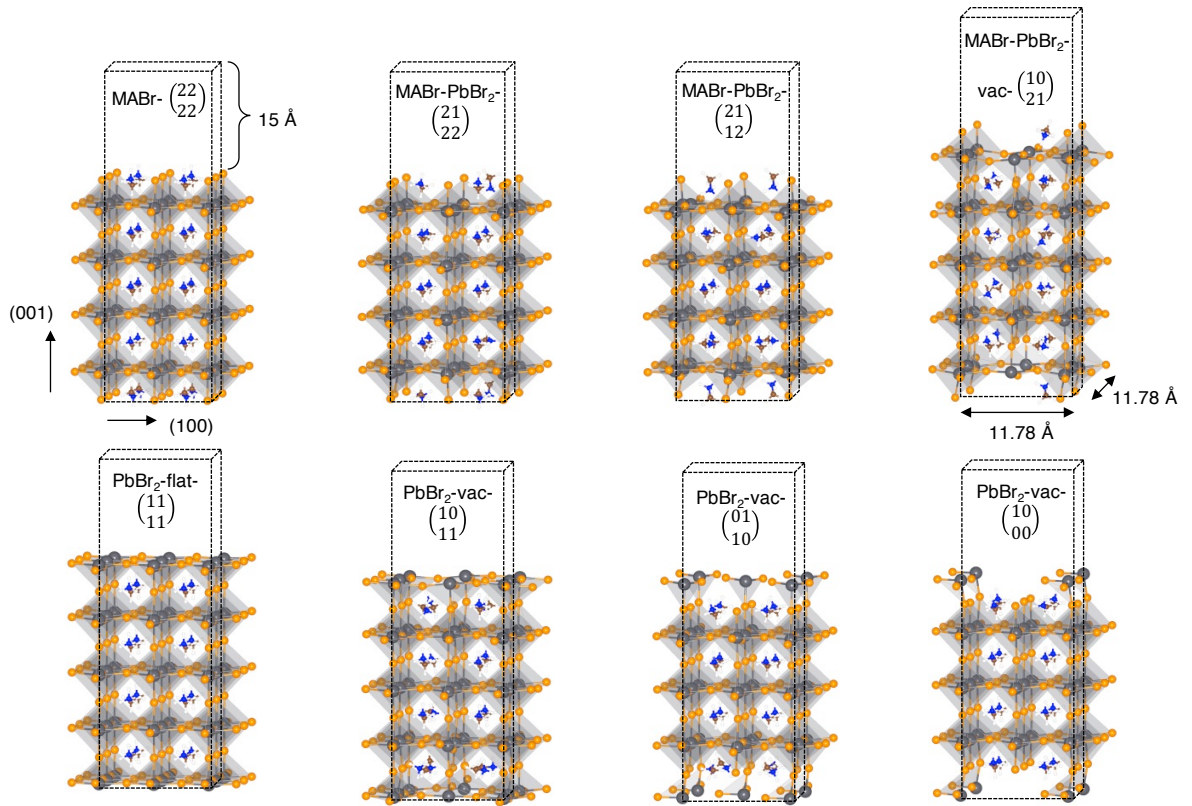


Figure 3. Side views of the full-size models for the surface formation energy calculations.

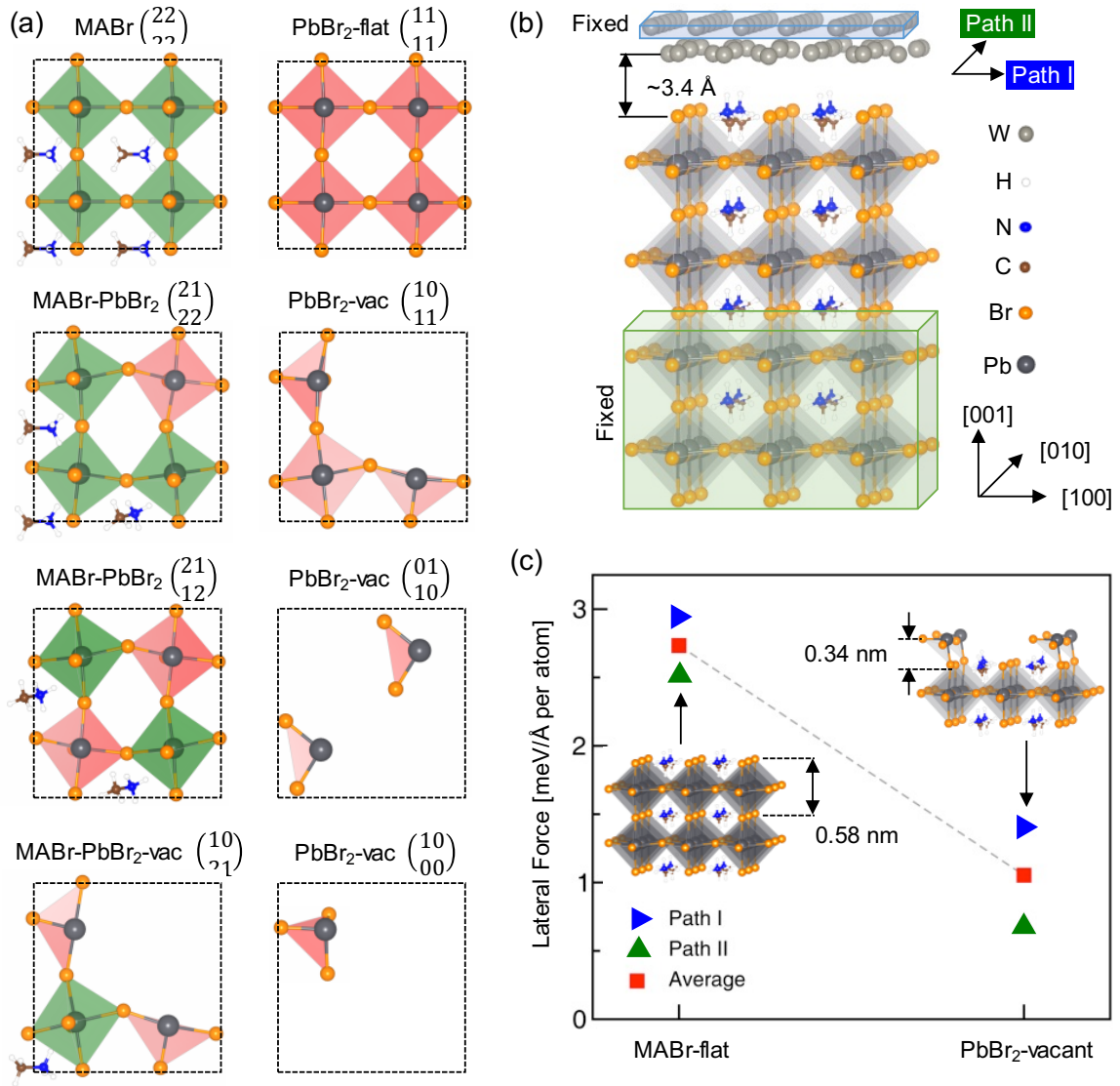


Figure 4. Atomic geometries showing the topmost layer of the stable surface terminations and the lateral friction force calculation mechanism. (a) Different possibilities for the atomic structures to simulate a freshly cleaved surface. The surface heights of these terminations are comparable to those measured in the experimental topographic images. Light green indicates full octahedral together with the MA ligand, light red shows half octahedra (PbBr_2), and the empty white space marks vacancies in the topmost layer inside the super cell boundary. (b) A schematic showing the setup for the lateral friction force calculations by sliding the tungsten tip over the perovskite surface along different paths. (c) Atomic-level first-principles friction results for the two most-stable surface terminations. The optimized structures of those stable MAPbBr_3 perovskite (001) surface terminations are shown in the inset.

We now discuss DFT calculation results and establish the correlations between atomic-scale morphologies of different MAPbBr_3 surface terminations and their frictions. We previously found that the MABr-flat and PbBr_2 -vacant surfaces are energetically the most

stable terminations with surface formation energies, $\Delta\Omega$, of $-39.9 \text{ meV}/\text{\AA}^2$ ($-29.3 \text{ meV}/\text{\AA}^2$) and $-15.5 \text{ meV}/\text{\AA}^2$ ($-9.1 \text{ meV}/\text{\AA}^2$), respectively, within the PBEsol³² (DFT-D3³³) exchange-correlation functional level.²³ Expanding our earlier work, we explored diverse MAPbBr₃(001) surface models more systematically; we show in Figure 3 and Figure 4(a) the side views of the full-size models and the topmost surface compositions respectively (see Table S1 for lattice parameters). The calculated formation energy values of different MAPbBr₃ surfaces in Table 1 show that, starting from the energetically most stable MABr-flat surface, the creation of PbBr₂ tetrahedra increase the surface energy by about 20 to 25 $\text{meV}/\text{\AA}^2$ per PbBr₂ tetrahedron. Overall, we conclude that many different surface terminations can exist, composed of a mixture of MABr, PbBr₂, and vacancy structural motives with comparable surface energies, which explains the experimental observation of different surface morphologies shown in Figures 1(a) and 2(a).

Table 1. Stability of various MAPbBr₃ (001) surfaces' termination configurations shown in Figures 3 and 4(a).

Surface Type	Surface Energy [$\text{meV}/\text{\AA}^2$]	
	PBEsol	DFT-D3
MABr-flat $\begin{pmatrix} 22 \\ 22 \end{pmatrix}$	-39.9	-29.3
MABr-PbBr ₂ $\begin{pmatrix} 21 \\ 22 \end{pmatrix}$	-14.9	-7.69
MABr-PbBr ₂ $\begin{pmatrix} 21 \\ 12 \end{pmatrix}$	6.05	12.0
MABr-PbBr ₂ -vacant $\begin{pmatrix} 10 \\ 21 \end{pmatrix}$	8.18	15.1
PbBr ₂ -flat $\begin{pmatrix} 11 \\ 11 \end{pmatrix}$	56.0	52.2
PbBr ₂ -vacant $\begin{pmatrix} 10 \\ 11 \end{pmatrix}$	31.6	34.7
PbBr ₂ -vacant $\begin{pmatrix} 01 \\ 10 \end{pmatrix}$	11.3	18.1
PbBr ₂ -vacant $\begin{pmatrix} 10 \\ 00 \end{pmatrix}$	-15.5	-9.06

We next analyzed the lateral frictional behavior for the two most stable MABr-flat and PbBr₂-vacant surfaces. Figure 4(b) depicts the atomistic model used for the friction calculations, in which a tip–surface layer sliding model was adopted.^{44,45} We slid the tungsten tip modeled as (001) bilayer along the paths I ([100] direction) and II ([010] direction), and as shown in Figure 4(c) obtained the average lateral forces of 2.73 and 1.05 meV/Å per atom for the stable MABr-flat and PbBr₂-vacant surfaces, respectively. In both the force magnitudes along the individual sliding paths and their averages, we consistently found that the MABr-flat termination exhibits a larger lateral force compared with the PbBr₂-vacant surface. We also compared the energy corrugation, lateral force, and shear strength $\tau_L = |f_L/A|$ for the stable surfaces, and, as summarized in Table 2, they show similar trends as the lateral forces. We emphasize that, while the numerical values of the computed lateral forces cannot be quantitatively compared with the experimental values (because of various factors such as the unknown actual composition of different surface structural motives in measured samples), our calculated results are consistent with the experimental assignment of the MABr-flat and PbBr₂-vacant surfaces as the high- and low-friction surfaces, respectively (mapping of Figure 1(c) to the configuration of Figures 1(d) and (e)). The smaller lateral forces in the PbBr₂-vacant can be understood in terms of several factors that include fewer atoms that establish contacts, the flexible nature of PbBr₂ tetrahedra with nearby vacancies, and the inert nature of the PbBr₂ species that will lead to very weak interactions with the tip. On the other hand, with the presence of organic MA groups at the interfaces could lead to stronger interactions with the tip and result in high friction, similar to graphene oxide producing higher friction than pristine graphene.^{45,46}

Table 2. Lateral force and shear strength of the two most stable MAPbBr₃ (001) surface terminations

Surface Type	Energy Corrugation [meV/atom]			Lateral Friction Force [meV/Å per atom]			Shear Strength [GPa]		
	Path I	Path II	Average	Path I	Path II	Average	Path I	Path II	Average
MABr	5.24	2.93	4.08	2.94	2.52	2.73	2.14	1.83	1.98
PbBr ₂ -vac	2.25	1.02	1.63	1.41	0.70	1.05	1.02	0.51	0.76

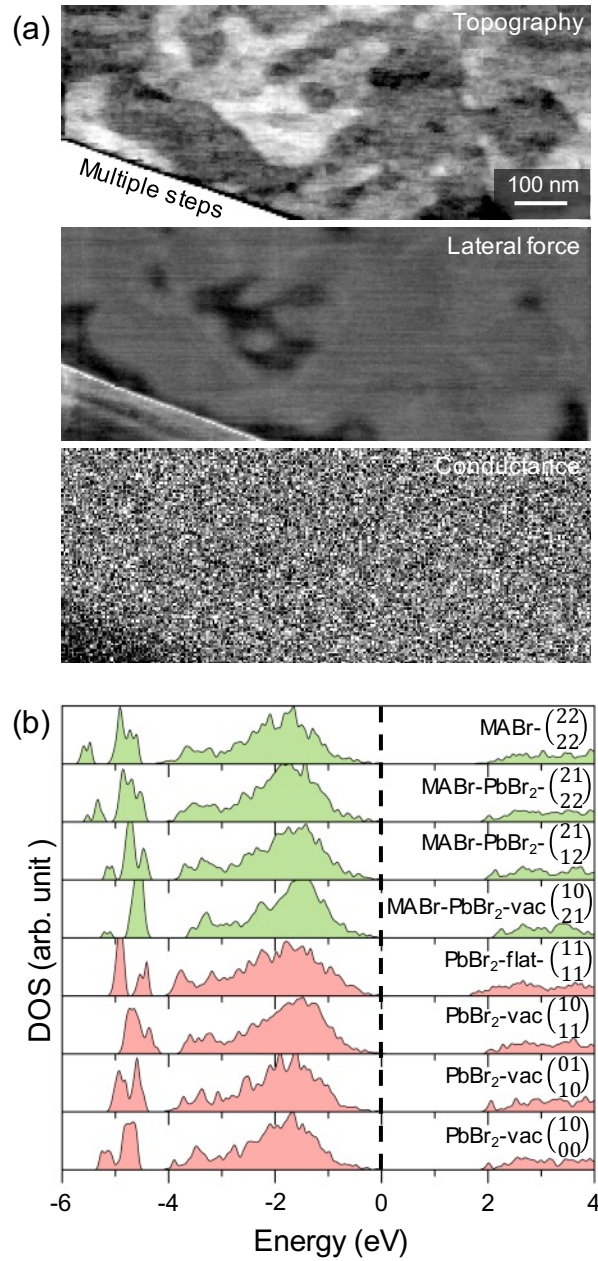


Figure 5. (a) AFM topography (top), lateral force (middle), and conductance (bottom) images obtained simultaneously at a sample bias of +1.5 V. The conductance image goes from -80 pA to 70 pA. (b) The density of states for the different surface terminations of MAPbBr₃. The top four DOS (green) indicate the surfaces that contain complete octahedra (MABr-flat), while the bottom four (red) mark the surfaces which have only half octahedra and vacancies (PbBr₂-vacant). The valence band maximum is set to zero.

In Figures 5(a) and (b), we analyzed the electronic structure of the surface domains of the MAPbBr₃ crystal. Figure 5(a) shows the topography (top), lateral force (middle), and conductance (bottom) AFM images obtained simultaneously at a sample bias of + 1.5 V. The

topography and the lateral force images show different surface domains, similar to Figures 2(a) and (b). In Figure 5(c), we do not observe notable differences in the conductance image depending on the surface domains of MAPbBr₃, indicating that the electronic structure does not significantly vary depending on the possible surface structures suggested in Figure 4(a). Indeed, as shown in Figure 5(b), the calculated density of states (DOS) reveal that the electronic states of MAPbBr₃ do not change much with surface defects. The PBEsol level band gaps of the considered models are provided in Table 3. Because of the stable nature of MABr-flat, PbBr₂-vacant, and other surface termination structures presented in Figure 4(a), their DOS do not exhibit midgap defect states and should enable a slow electron–hole recombination rate. Based on our results, we thus predict that any stable surface termination of MAPbBr₃ perovskite (Figure 4(a)) will be a suitable candidate to be included in high-performance and stable optical devices.

Table 3. PBEsol level band gaps of different MAPbBr₃ (001) surfaces terminations.

Surface Type	Band gap [eV]
MABr-flat $\begin{pmatrix} 22 \\ 22 \end{pmatrix}$	1.66
MABr-PbBr ₂ $\begin{pmatrix} 21 \\ 22 \end{pmatrix}$	1.80
MABr-PbBr ₂ $\begin{pmatrix} 21 \\ 12 \end{pmatrix}$	1.87
MABr-PbBr ₂ -vacant $\begin{pmatrix} 10 \\ 21 \end{pmatrix}$	2.11
PbBr ₂ -flat $\begin{pmatrix} 11 \\ 11 \end{pmatrix}$	1.54
PbBr ₂ -vacant $\begin{pmatrix} 10 \\ 11 \end{pmatrix}$	1.89
PbBr ₂ -vacant $\begin{pmatrix} 01 \\ 10 \end{pmatrix}$	1.81
PbBr ₂ -vacant $\begin{pmatrix} 10 \\ 00 \end{pmatrix}$	1.81

CONCLUSIONS

To conclude, we observed the formation of a stable MABr-flat terminated surface structure that is similar to its bulk structure with less-preferred full and partial PbBr_2 -terminated surface with PbBr_2 vacancies (namely PbBr_2 -vacant termination) co-existing after cleavage of a MAPbBr_3 single crystal in UHV. Energetically, the MABr-flat surface termination exhibits the lowest surface formation energy, but we show that a mixture of MABr, PbBr_2 , and PbBr_2 -poor vacant surface terminations could coexist locally. Through DFT calculations and AFM topography and friction observations, we show distinctive terrace heights and friction contrast along the freshly cleaved surface that originated from different surface terminations. The MABr-flat termination exhibits a distinctively higher friction coefficient compared with the PbBr_2 -vacant termination with PbBr_2 vacancies. The electronic structure of the MAPbBr_3 surfaces revealed no mid-gap states for all surface terminations considered herein, suggesting single-crystal MAPbBr_3 as a promising candidate for photovoltaic applications.

ASSOCIATED CONTENT

Supporting Information

AFM images of large terraces of MAPbBr₃ and the calculated lattice constants (PDF).

AUTHOR INFORMATION

Corresponding Authors

*Email: Yabing.Qi@OIST.jp

*Email: y.h.kim@kaist.ac.kr

*Email: jeongypark@kaist.ac.kr

Author contributions

‡J.I.J. Choi and M.E. Khan have contributed equally to this work.

Competing interests

The authors declare no competing financial interests.

ACKNOWLEDGEMENTS

J.I.J.C., H.L., and J.Y.P. were supported by the Institute for Basic Science of Korea (IBS-R004). M.E.K. and Y.-H.K. were supported by the Basic Research Program (2017R1A2B3009872), Nano-Material Technology Development Program (2016M3A7B4024133), Global Frontier Program (2013M3A6B1078881), and Basic Research Lab Program (2017R1A4A1015400) of the National Research Foundation of Korea. Z. H., L.

K. O., and Y. B. Q. acknowledge funding support from the Energy Materials and Surface Sciences Unit of the Okinawa Institute of Science and Technology Graduate University, the OIST R&D Cluster Research Program, the OIST Proof of Concept (POC) Program, and JSPS KAKENHI Grant Number JP18K05266.

REFERENCES

- (1) Xing, G.; Mathews, N.; Sun, S.; Lim, S. S.; Lam, Y. M.; Gratzel, M.; Mhaisalkar, S.; Sum, T. C. Long-Range Balanced Electron- and Hole-Transport Lengths in Organic-Inorganic $\text{CH}_3\text{NH}_3\text{PbI}_3$. *Science* **2013**, *342*, 344–347.
- (2) Stranks, S. D.; Eperon, G. E.; Grancini, G.; Menelaou, C.; Alcocer, M. J. P.; Leijtens, T.; Herz, L. M.; Petrozza, A.; Snaith, H. J. Electron-Hole Diffusion Lengths Exceeding 1 Micrometer in an Organometal Trihalide Perovskite Absorber. *Science* **2013**, *342*, 341–344.
- (3) Stoumpos, C. C.; Malliakas, C. D.; Kanatzidis, M. G. Semiconducting Tin and Lead Iodide Perovskites with Organic Cations: Phase Transitions, High Mobilities, and Near-Infrared Photoluminescent Properties. *Inorg. Chem.* **2013**, *52*, 9019–9038.
- (4) Edri, E.; Kirmayer, S.; Mukhopadhyay, S.; Gartsman, K.; Hodes, G.; Cahen, D. Elucidating the Charge Carrier Separation and Working Mechanism of $\text{CH}_3\text{NH}_3\text{PbI}_{3-x}\text{Cl}_x$ Perovskite Solar Cells. *Nat. Commun.* **2014**, *5*, 3461.
- (5) Wehrenfennig, C.; Eperon, G. E.; Johnston, M. B.; Snaith, H. J.; Herz, L. M. High Charge Carrier Mobilities and Lifetimes in Organolead Trihalide Perovskites. *Adv. Mater.* **2014**, *26*, 1584–1589.
- (6) Yin, W.-J.; Shi, T.; Yan, Y. Unusual Defect Physics in $\text{CH}_3\text{NH}_3\text{PbI}_3$ Perovskite Solar Cell Absorber. *Appl. Phys. Lett.* **2014**, *104*, 063903.
- (7) Liu, M.; Johnston, M. B.; Snaith, H. J. Efficient Planar Heterojunction Perovskite Solar Cells by Vapour Deposition. *Nature* **2013**, *501*, 395–398.
- (8) Park, N.-G. Organometal Perovskite Light Absorbers toward a 20% Efficiency Low-Cost Solid-State Mesoscopic Solar Cell. *J. Phys. Chem. Lett.* **2013**, *4*, 2423–2429.
- (9) Tan, Z.-K.; Moghaddam, R. S.; Lai, M. L.; Docampo, P.; Higler, R.; Deschler, F.; Price, M.; Sadhanala, A.; Pazos, L. M.; Credgington, D.; et al. Bright Light-Emitting Diodes Based on Organometal Halide Perovskite. *Nat. Nanotechnol.* **2014**, *9*, 687–692.
- (10) Jeon, N. J.; Noh, J. H.; Yang, W. S.; Kim, Y. C.; Ryu, S.; Seo, J.; Seok, S. I. Compositional Engineering of Perovskite Materials for High-Performance Solar Cells. *Nature* **2015**, *517*, 476–480.
- (11) Cho, H.; Jeong, S.-H.; Park, M.-H.; Kim, Y.-H.; Wolf, C.; Lee, C.-L.; Heo, J. H.; Sadhanala, A.; Myoung, N.; Yoo, S.; et al. Overcoming the Electroluminescence Efficiency Limitations of Perovskite Light-Emitting Diodes. *Science* **2015**, *350*, 1222–1225.
- (12) Chin, X. Y.; Cortecchia, D.; Yin, J.; Bruno, A.; Soci, C. Lead Iodide Perovskite Light-Emitting Field-Effect Transistor. *Nat. Commun.* **2015**, *6*, 7383.
- (13) Xiao, Z.; Kerner, R. A.; Zhao, L.; Tran, N. L.; Lee, K. M.; Koh, T.-W.; Scholes, G. D.; Rand, B. P. Efficient Perovskite Light-Emitting Diodes Featuring Nanometre-Sized Crystallites. *Nat. Photonics* **2017**, *11*, 108–115.
- (14) Yin, W.-J.; Shi, T.; Yan, Y. Unique Properties of Halide Perovskites as Possible Origins of the Superior Solar Cell Performance. *Adv. Mater.* **2014**, *26*, 4653–4658.
- (15) Frost, J. M.; Butler, K. T.; Brivio, F.; Hendon, C. H.; van Schilfhaarde, M.; Walsh, A. Atomistic Origins of High-Performance in Hybrid Halide Perovskite Solar Cells. *Nano Lett.* **2014**, *14*, 2584–2590.
- (16) Shi, T.; Yin, W.-J.; Hong, F.; Zhu, K.; Yan, Y. Unipolar Self-Doping Behavior in Perovskite $\text{CH}_3\text{NH}_3\text{PbBr}_3$. *Appl. Phys. Lett.* **2015**, *106*, 103902.
- (17) Buin, A.; Comin, R.; Xu, J.; Ip, A. H.; Sargent, E. H. Halide-Dependent Electronic Structure of Organolead Perovskite Materials. *Chem. Mater.* **2015**, *27*, 4405–4412.

- (18) Motta, C.; El-Mellouhi, F.; Kais, S.; Tabet, N.; Alharbi, F.; Sanvito, S. Revealing the Role of Organic Cations in Hybrid Halide Perovskite $\text{CH}_3\text{NH}_3\text{PbI}_3$. *Nat. Commun.* **2015**, *6*, 7026.
- (19) Somorjai, G. A.; York, R. L.; Butcher, D.; Park, J. Y. The Evolution of Model Catalytic Systems; Studies of Structure, Bonding and Dynamics from Single Crystal Metal Surfaces to Nanoparticles, and from Low Pressure ($<10^{-3}$ Torr) to High Pressure ($>10^{-3}$ Torr) to Liquid Interfaces. *Phys. Chem. Chem. Phys.* **2007**, *9*, 3500–3513.
- (20) Somorjai, G. A.; Park, J. Y. Molecular Surface Chemistry by Metal Single Crystals and Nanoparticles from Vacuum to High Pressure. *Chem. Soc. Rev.* **2008**, *37*, 2155.
- (21) Somorjai, G. A.; Park, J. Y. Concepts, Instruments, and Model Systems That Enabled the Rapid Evolution of Surface Science. *Surf. Sci.* **2009**, *603*, 1293–1300.
- (22) Ohmann, R.; Ono, L. K.; Kim, H.-S.; Lin, H.; Lee, M. V.; Li, Y.; Park, N.-G.; Qi, Y. Real-Space Imaging of the Atomic Structure of Organic–Inorganic Perovskite. *J. Am. Chem. Soc.* **2015**, *137*, 16049–16054.
- (23) Choi, J. I. J.; Khan, M. E.; Hawash, Z.; Kim, K. J.; Lee, H.; Ono, L. K.; Qi, Y.; Kim, Y.-H.; Park, J. Y. Atomic-Scale View of Stability and Degradation of Single-Crystal MAPbBr_3 Surfaces. *J. Mater. Chem. A* **2019**, *7*, 20760–20766.
- (24) Park, J. Y.; Salmeron, M. Fundamental Aspects of Energy Dissipation in Friction. *Chem. Rev.* **2014**, *114*, 677–711.
- (25) Saidaminov, M. I.; Abdelhady, A. L.; Murali, B.; Alarousu, E.; Burlakov, V. M.; Peng, W.; Dursun, I.; Wang, L.; He, Y.; Maculan, G.; et al. High-Quality Bulk Hybrid Perovskite Single Crystals within Minutes by Inverse Temperature Crystallization. *Nat. Commun.* **2015**, *6*, 7586.
- (26) Park, J. Y.; Maier, S.; Hendriksen, B.; Salmeron, M. Sensing Current and Forces with SPM. *Mater. Today* **2010**, *13*, 38–45.
- (27) Kwon, S.; Choi, S.; Chung, H. J.; Yang, H.; Seo, S.; Jhi, S.-H.; Young Park, J. Probing Nanoscale Conductance of Monolayer Graphene under Pressure. *Appl. Phys. Lett.* **2011**, *99*, 013110.
- (28) Choi, J. I. J.; Kim, J. J.; Oh, W.; Doh, W. H.; Park, J. Y. Ambient-Pressure Atomic Force Microscope with Variable Pressure from Ultra-High Vacuum up to One Bar. *Rev. Sci. Instrum.* **2018**, *89*, 103701.
- (29) Khan, M. E.; Lee, J.; Byeon, S.; Kim, Y.-H. Semimetallicity and Negative Differential Resistance from Hybrid Halide Perovskite Nanowires. *Adv. Funct. Mater.* **2019**, *29*, 1807620.
- (30) Kresse, G.; Hafner, J. *Ab Initio* Molecular Dynamics for Liquid Metals. *Phys. Rev. B* **1993**, *47*, 558–561.
- (31) Kresse, G.; Hafner, J. *Ab Initio* Molecular-Dynamics Simulation of the Liquid-Metal–Amorphous-Semiconductor Transition in Germanium. *Phys. Rev. B* **1994**, *49*, 14251–14269.
- (32) Perdew, J. P.; Ruzsinszky, A.; Csonka, G. I.; Vydrov, O. A.; Scuseria, G. E.; Constantin, L. A.; Zhou, X.; Burke, K. Restoring the Density-Gradient Expansion for Exchange in Solids and Surfaces. *Phys. Rev. Lett.* **2008**, *100*, 136406.
- (33) Grimme, S.; Antony, J.; Ehrlich, S.; Krieg, H. A Consistent and Accurate *Ab Initio* Parametrization of Density Functional Dispersion Correction (DFT-D) for the 94 Elements H–Pu. *J. Chem. Phys.* **2010**, *132*, 154104.
- (34) Blöchl, P. E. Projector Augmented-Wave Method. *Phys. Rev. B* **1994**, *50*, 17953.
- (35) Kresse, G.; Joubert, D. From Ultrasoft Pseudopotentials to the Projector Augmented-Wave Method. *Phys. Rev. B* **1999**, *59*, 1758–1775.

- (36) Poglitsch, A.; Weber, D. Dynamic Disorder in Methylammoniumtrihalogenoplumbates (II) Observed by Millimeter-Wave Spectroscopy. *J. Chem. Phys.* **1987**, *87*, 6373–6378.
- (37) Chien, T. Y.; Chakhalian, J.; Freeland, J. W.; Guisinger, N. P. Cross-Sectional Scanning Tunneling Microscopy Applied to Complex Oxide Interfaces. *Adv. Funct. Mater.* **2013**, *23*, 2565–2575.
- (38) Setvin, M.; Reticcioli, M.; Poelzleitner, F.; Hulva, J.; Schmid, M.; Boatner, L. A.; Franchini, C.; Diebold, U. Polarity Compensation Mechanisms on the Perovskite Surface $\text{KTaO}_3(001)$. *Science* **2018**, *359*, 572–575.
- (39) Sokolović, I.; Schmid, M.; Diebold, U.; Setvin, M. Incipient Ferroelectricity: A Route towards Bulk-Terminated SrTiO_3 . *Phys. Rev. Mater.* **2019**, *3*, 034407.
- (40) Johnson, K. L.; Kendall, K.; Roberts, A. D. Surface Energy and the Contact of Elastic Solids. *Proc. R. Soc. Math. Phys. Eng. Sci.* **1971**, *324*, 301–313.
- (41) Derjaguin, B. V.; Muller, V. M.; Toporov, Yu. P. Effect of Contact Deformations on the Adhesion of Particles. *J. Colloid Interface Sci.* **1975**, *53*, 314–326.
- (42) Carpick, R. W.; Ogletree, D. F.; Salmeron, M. A General Equation for Fitting Contact Area and Friction vs Load Measurements. *J. Colloid Interface Sci.* **1999**, *211*, 395–400.
- (43) Rakita, Y.; Cohen, S. R.; Kedem, N. K.; Hodes, G.; Cahen, D. Mechanical Properties of APbX_3 (A = Cs or CH_3NH_3 ; X = I or Br) Perovskite Single Crystals. *MRS Commun.* **2015**, *5*, 623–629.
- (44) Liang, T.; Sawyer, W. G.; Perry, S. S.; Sinnott, S. B.; Phillpot, S. R. First-Principles Determination of Static Potential Energy Surfaces for Atomic Friction in MoS_2 and MoO_3 . *Phys. Rev. B* **2008**, *77*, 104105.
- (45) Wang, L.-F.; Ma, T.-B.; Hu, Y.-Z.; Wang, H. Atomic-Scale Friction in Graphene Oxide: An Interfacial Interaction Perspective from First-Principles Calculations. *Phys. Rev. B* **2012**, *86*, 125436.
- (46) Byun, I.-S.; Yoon, D.; Choi, J. S.; Hwang, I.; Lee, D. H.; Lee, M. J.; Kawai, T.; Son, Y.-W.; Jia, Q.; Cheong, H.; et al. Nanoscale Lithography on Monolayer Graphene Using Hydrogenation and Oxidation. *ACS Nano* **2011**, *5*, 6417–6424.